AGU PUBLICATIONS

Water Resources Research

TECHNICAL REPORTS: METHODS

10.1002/2017WR021032

Fracture network created by 3-D printer and its validation using CT images

Anna Suzuki[1,2], Noriaki Watanabe[3], Kewen Li[1], and Roland N. Horne[1]

[1]Department of Energy Resources Engineering, Stanford University, Stanford, California, USA, [2]Institute of Fluid Science, Tohoku University, Miyagi, Japan, [3]Department of Environmental Studies for Advanced Society, Graduate School of Environmental Studies, Tohoku University, Sendai, Japan

Key Points:
- The accuracy of creating fracture networks by 3-D was verified by a X-ray CT scanner
- Use of hexane after printing was found to be an effective way to remove wax for the posttreatment
- The experimental value of permeability was close to the equivalent value of numerical results

Supporting Information:
- Supporting Information S1

Correspondence to:
A. Suzuki,
anna.suzuki@tohoku.ac.jp

Citation:
Suzuki, A., N. Watanabe, K. Li, and R. N. Horne (2017), Fracture network created by 3-D printer and its validation using CT images, *Water Resour. Res.*, *53*, doi:10.1002/2017WR021032.

Received 30 APR 2017
Accepted 30 JUN 2017
Accepted article online 6 JUL 2017

Abstract Understanding flow mechanisms in fractured media is essential for geoscientific research and geological development industries. This study used 3-D printed fracture networks in order to control the properties of fracture distributions inside the sample. The accuracy and appropriateness of creating samples by the 3-D printer was investigated by using a X-ray CT scanner. The CT scan images suggest that the 3-D printer is able to reproduce complex three-dimensional spatial distributions of fracture networks. Use of hexane after printing was found to be an effective way to remove wax for the posttreatment. Local permeability was obtained by the cubic law and used to calculate the global mean. The experimental value of the permeability was between the arithmetic and geometric means of the numerical results, which is consistent with conventional studies. This methodology based on 3-D printed fracture networks can help validate existing flow modeling and numerical methods.

1. Introduction

Fluid flow within fractured rocks is controlled strongly by three-dimensional geometry of the fractures. Several approaches to model fluid flow in fractured media have been proposed: Mathematical modeling using a continuum approach solves the general mass and energy conservation equations. The approach represents flow in a fractured medium by providing an equivalent permeability for overlapping fracture/matrix domains [e.g., *Neuman*, 1988; *Tsang et al.*, 1996]. A dual-continuum method (i.e., dual-porosity, dual-permeability, and more general multiple-continua models) expresses fracture-matrix interactions by introducing overlapping continua [e.g., *Warren and Root*, 1963; *Pruess and Narasimhan*, 1985]. More detailed simulations with explicit fractures are conducted by discrete fracture networks (DFNs), which enables us to take local variation of structures into account [e.g., *Long et al.*, 1982; *Cacas et al.*, 1990].

Fracture structures in nature are complex and heterogeneous, and the invisibility of the internal structures makes it difficult to grasp their three-dimensional distributions. Certainly, internal structures of rock specimens can be observed in the laboratory (e.g., by X-ray Computed Tomography (CT) [*Ketcham and Carlson*, 2001]), however the imaging has limitations of the sample scales and only provides sample-specific structures. Considering upscaling to the field scale, because all fracture networks cannot be fully observed, it is absolutely necessary to derive bulk (equivalent) properties implicitly for generic networks.

Calculating equivalent (effective) permeability has been studied for several decades, as reviewed by, e.g., *Renard and de Marsily* [1997] and *Liu et al.* [2016]. There are two ways to determine equivalent permeability in fractured media. One is a deterministic approach by using DFNs to simulate flow in fracture networks [*Liu et al.*, 2016]. *Bour and Davy* [1997] used a percolation theory to derive the equivalent permeability in a fractured medium containing fractures of different lengths. *Leung and Zimmerman* [2012] developed a DFN composing fractures with different fracture lengths, which follows power law scaling. They led mathematically to the equivalent permeability of the power law scaling fractures. *Jafari and Babadagli* [2011] analyzed two-dimensional fracture distributions at outcrops and derived a regression equation for the equivalent permeability. *Liu et al.* [2015] and *Miao et al.* [2015] derived the equivalent permeability of randomly-distributed fracture networks.

Another method of calculating the equivalent permeability for heterogeneous systems is to obtain statistical values. There has been a strong practical requirement in the hydrology and oil recovery industries for

simple estimates. The geometric mean simply gives the closest estimate to the equivalent permeability for a random, isotropic distribution [*Warren and Price*, 1961] and is still taken as the standard estimate within the petroleum industry.

Basically, all research on the equivalent permeability remains theoretical, and there is no generic model of which the validity was demonstrated by laboratory experiment. Even if we use real rock samples in laboratory, the structure differs for each sample, so it is difficult to validate the theory and to develop generic models.

Based on the above, we propose an experimental method to validate theoretical studies and to examine effective methods for calculating equivalent permeability by using 3-D printed fracture network. 3-D printers are useful as rapid prototyping and small scale manufacturing devices. Their applications have become widespread in many research fields. In rock mechanics and mining engineering, *Ju et al*. [2014] and *Jiang et al*. [2016] created fracture samples using a 3-D printer and investigated the applicability to measuring mechanical properties. *Ishutov et al*. [2015] and *Head and Vanorio* [2016] created porous samples to measure petrophysical properties. They created samples by using CT scan images of real rock samples, which can reproduce the same geometries as the specific rock sample at the core scale. Although the 3-D printed rocks have clear difference from real rocks (i.e., zero permeability in rock matrix, and difference roughness of fracture surfaces), the 3-D printer can create fracture geometry of either actual distributions (i.e., CT scan images or outcrop photos) or any type of geometric models (i.e., geometric network or stochastic heterogeneity of petrophysical properties) repeatedly. The experimental results will help validate existing theory and numerical methods. In addition, 3-D printers allow us to control fracture geometries, which would provide understanding several aspects of flow mechanisms in fractured rocks.

Suzuki et al. [2016] created a fracture network model by using a 3-D printer and conducted flow tests. Because the 3-D printing process required the printing of wax inside the open pore space and removal of the wax after producing the 3-D products, ethanol was used to dissolve the wax during the posttreatment. However, the paper was not able to conclude that the use of ethanol is appropriate, in that the wax was not fully removed. Here, we used hexane to remove the wax as well as ethanol and examined the accuracy of the fracture network samples by CT scanning. The effectiveness of this posttreatment for fracture network creation is discussed. In addition, we measured the porosity and the permeability of the sample, and compared with the equivalent permeability calculated by numerical simulations with the same fracture network model.

2. Experimental Setup

2.1. Creating 3-D Printed Fracture Network

We used a 3-D printer (ProJet^{TM} HD 3000Plus, 3D Systems) at the Stanford 3-Dimensional Printing Facility, which uses the multijet modeling (MJM) method. The MJM is a rapid prototyping process that provides a quick turnaround for smooth, high-resolution, hard plastic parts with complex geometries. The official resolution of the printer is 16 μm. The accuracy is 0.025–0.05 mm per inch of part dimension, which may vary depending on build parameters, part geometry and size, part orientation, and postprocessing methods. The base material is UV curable acrylic plastic (VisiJet$^{®}$ EX200 Plastic Material), solidified by UV lamps. The material properties are listed in Table 1. The creation of void spaces (fractures) is achieved in such a device by printing the voids with wax, which needed to be removed from the inside of the sample after the printing.

Table 1. Material Properties for Printed Specimens

Properties	Value
Composition	UV Curable Acrylic Plastic
Density @ 80 deg C (liquid)	1.02 g/cm^3
Tensile Strength	42.4 MPa
Tensile Modulus	1283 MPa
Elongation at Break	6.83%
Flexural Modulus	1159 MPa
Izod Notched Impact	2.5 kJ/m^2
Glass Transition Temperature @1Hz	52.5 Tg

Before generating fracture network models, the smallest aperture was determined to be set as small as possible. We printed a rectangular block on which ten grooves were created with different widths (0.1, 0.13, 0.17, 0.2, 0.28, 0.35, 0.46, 0.60, 0.77, and 1.00 mm). Water was dripped on each groove. Water flowed through the apertures larger than 0.2 mm, while smaller apertures in the block did not pass water. Although the traces of smaller

aperture were observed, the apertures were not open. The publicized resolution, which is 16 microns, was clearly not achieved within the void structures inside the printed specimen. Thus, we used a minimum aperture of 0.2 mm in subsequent fabrications.

The 3-D printer creates various structures and provides many approaches that should be considered to understand the flow and transport phenomena. On the other hand, because only the parts from which the wax is removed become flow paths, the 3-D printer requires continuous fracture networks connected to the outside. This paper presents an example of systematic fracture sets with a large number of fractures, which led to high permeability and high porosity.

Disc-shaped fractures were generated with radii according to the power-law scaling with maximum and minimum radii [e.g., *Odling et al*., 1999; *Bour et al*., 2002; *Davy et al*., 2010]. The fracture aperture was specified to be proportional to its radius based on linear elastic fracture mechanics [*Vermilye and Scholz*, 1995]. As *Olson* [2003] and others [e.g., *Schultz et al*., 2013] demonstrated sublinear aperture-to-length scaling for opening mode cracks (i.e., joints, veins, and dikes) in field data, the systematic scaling relationship of the aperture-to-length and its flow properties is beyond the scope of this paper. The values of maximum and minimum radii were set to 1.6 mm and 8 mm, respectively. The maximum radius was set to 8 mm, which was less than a half of the sample diameter (1.27 cm), in order to prevent the fracture from penetrating through the sample. The ratio of fracture aperture to the length was set to 0.125, which was determined due to the limitation of the sample sizes and the precision of the 3-D printer. The value was consistent with field data in the range between 10^{-4} and 0.2 shown in *Schultz et al*. [2013]. Fractures were allowed to cross each other in this study, while propagating fractures commonly become deflected into and often arrested at the discontinuities. Further work is in progress where fractures are nucleating and growing simultaneously, as suggested by *Davy et al*. [2010]. Although spatial correlation of fractures could be controlled by some systematic functions, such as two-point correlation function for positions [*Bour and Davy*, 1999], fracture positions and their orientations randomly distributed in this study need to be reconstructed to account for natural correlated and anisotropic fracture systems.

The cluster of fractures is shown in Figure 1a. A solid cylinder subtracted the cluster of fractures to create a fracture network (Figure 1b). The cylinder was of height 4 cm and diameter 2.54 cm. The core holder cladding was also printed as part of the unit object to bound the sides of the cylinder and prevent water leak (Figure 1c). The thickness of the core holder cladding was 0.635 cm. A STL file including the surface geometry of the three-dimensional fracture network was sent to the 3-D printer. We used a 3D CAD modeling software called "OpenSCAD," which compiles and renders the structure into the STL format.

After printing, normal posttreatment is to immerse the samples in a heated ultrasonic oil bath to melt the wax away. The models were submerged in hot water at 60°C first and shaken for approximately an hour so that the wax melted and floated up through the holes. Note that the melting points of the wax is 55–65°C (VisiJet® EX200 Plastic Material) and a general heat softening temperature of UV curable acrylic plastic for the MJM method is 80°C [*Olasek and Wiklak*, 2014]. Because heating and shaking the samples did not remove all of wax, we used ethanol or hexane to dissolve the wax. We heated up the sample in water at 60°C first to liquefy the wax then quickly pumped the ethanol or hexane through the sample overnight. Then isopropyl alcohol was used to flush the sample to dissolve the ethanol and the hexane.

2.2. CT Scanning

Assessing the accuracy and appropriateness of the samples was conducted by comparisons of the cross sections between the computational designs and the 3-D printed samples. The images of cross sections of the STL file were generated by a visualization software, Autodesk® Netfabb. In contrast, the cross sections of the 3-D printed samples were obtained by X-ray CT scanning. The X-ray CT scanning was performed using the ScanXmate-D225RSS270 (Comscantecno Co., Ltd.). The parametric properties of the CT scanner are summarized in Table 2. The CT scanner provides a three-dimensional distribution of CT values and the cross sections with a voxel resolution of 35 μm. The sample was completely dry during CT scanning. The CT numbers are measured with a certain range of distribution. Average values of CT numbers were obtained from each histogram. The CT number for air was -1000 HU, while the averages of CT number for plastic, wax, and liquid for posttreatment (i.e., water, ethanol, hexane, and isopropyl alcohol) were higher than -400, as listed in Table 2. Because we observed that the distributions of CT numbers for wax and plastic overlapped, it is difficult to determine a threshold of CT numbers for wax and plastic. In contrast, there was a clear threshold

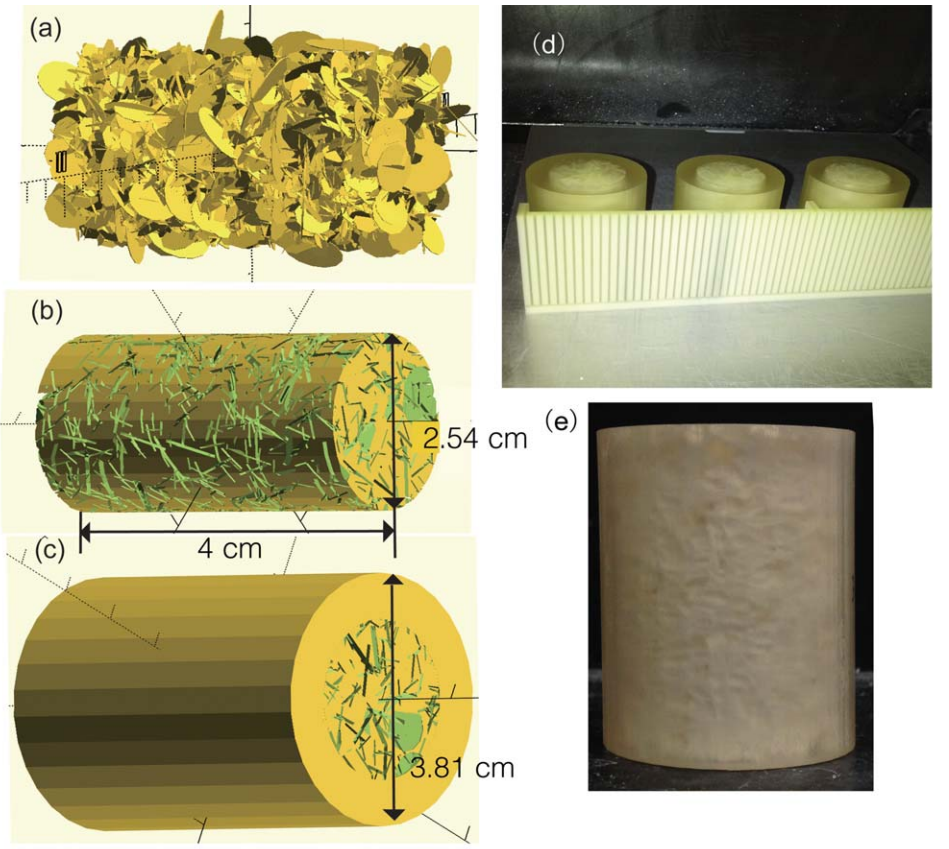

Figure 1. (a) A cluster of fracture network, (b) a solid cylinder subtracting fractures, (c) a model with cladding, (d) printing samples in 3-D printer, and (e) 3-D printed sample.

between the CT number of air and that of other materials. Thus, we can distinguish the void spaces (air) in the sample by using CT images.

2.3. Flow Experiment

After removing the wax, the sample was used to conduct flow experiments to obtain a measurement of the permeability. The sample was immersed in water under vacuum for full saturation. The water was injected into the sample by constant hydraulic head difference.

Spider connections were used at the inlet and the outlet to achieve homogeneous, spatially distributed injection. In order to examine dependence of flux, the elevation of the water source was set successively to 28, 56, and 114 cm. Pressure difference showed a linear relationship with the flow rate, as suggested by Darcy's law. The flow rate was obtained by the weight history of water at the outlet. The permeability in the flow direction was obtained from the ratio between pressure difference and the flow rate (and viscosity) in Darcy's law.

Table 2. The Parameter Values of the X-Ray CT Scanner[a]

Parameter	Parameter Value
X-ray tube voltage	120 kV
X-ray tube current	300 μA
Voxel resolution	35.009 μm
CT number for water	0 HU
CT number for air	−1000 HU
CT number for wax (average)	−73 HU
CT number for plastic (average)	27 HU
CT number for ethanol (average)	−310 HU
CT number for hexane (average)	−318 HU
CT number for isopropyl alcohol (average)	−326 HU

[a]The ScanXmate-D225RSS270, Comscantecno Co., Ltd. The acquisition of the average of CT values is described in supporting information S1.

3. Numerical Calculation for Hydraulic Properties

Fracture flow has been modeled as viscous flow between two parallel plates, which is governed by the well-known "cubic law" [*Bear*, 1972; *Witherspoon et al.*, 1980]. Because the permeability depends on fracture aperture, variations of fracture apertures provide

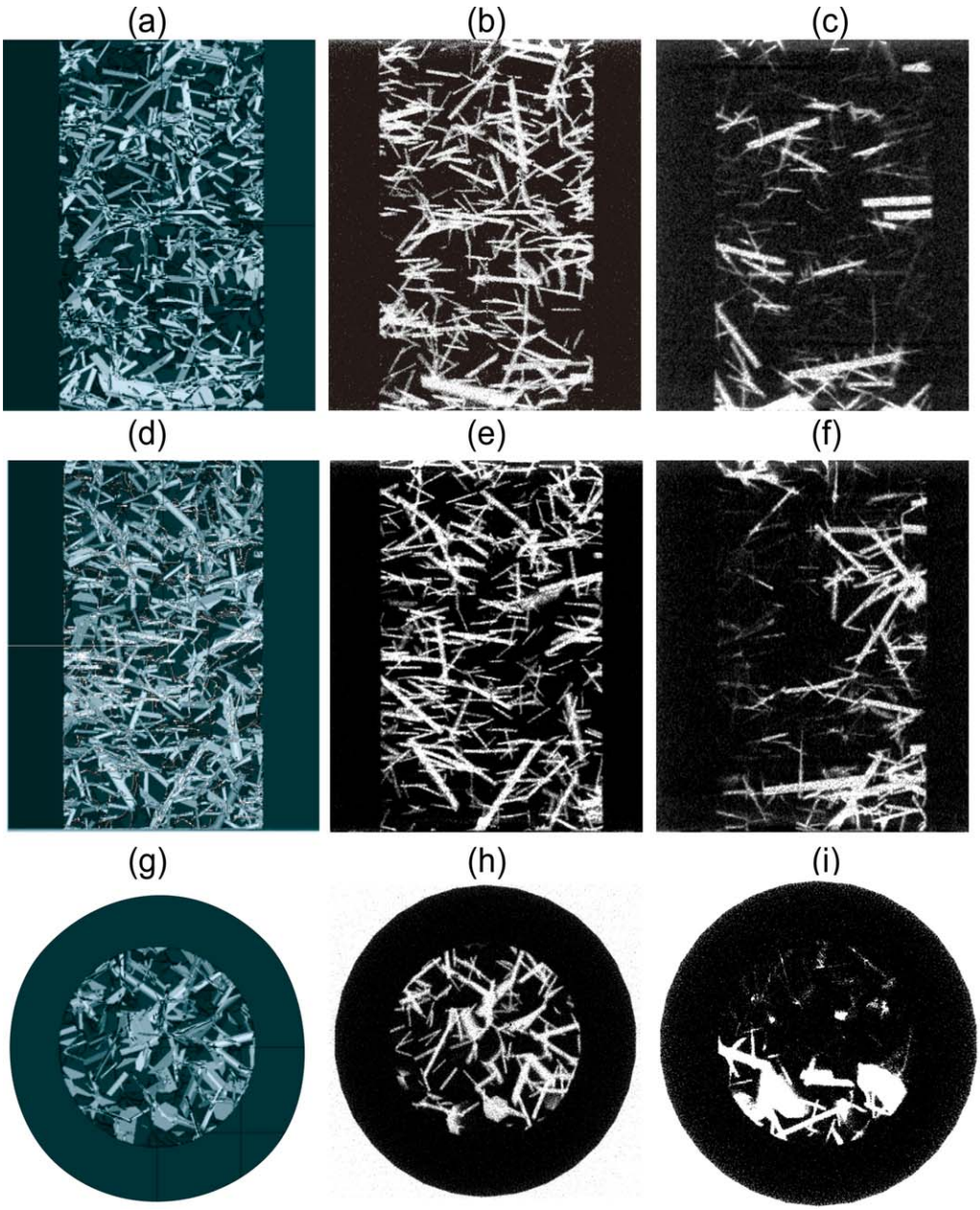

Figure 2. (a, d, g) Cross sections of the computational designs, (b, e, h) CT images of the 3-D printed sample treated with hexane, and (c, f, i) CT images of the 3-D printed sample treated with ethanol: (a–c) ZX slices, (d, e) YZ slices, (g–i) XY slices at the center.

localized heterogeneities of permeability. When the permeability is used in numerical models, the variations are normally replaced with averaged or upscaled quantities. Several papers have suggested that the geometric mean can give good results for the equivalent permeability under certain conditions [e.g., *Dagan*, 1989] and this mean is still taken as the standard estimate within the petroleum industry. Thus, we calculated averaged values from the local permeability obtained from the cubic law, and examined the effectiveness of the geometric means for the local permeability.

Experimental permeability was compared with the numerical values based on the original computational geometries as shown in Figure 2a. Flow experiments using the printed fracture network provided the permeability in the longitudinal direction. In order to compare with the experimental permeability, we generated the permeability tensor in a numerical model with cubic lattice grids. The calculation area was divided into lattice grids in the numerical model. We used coarse grids (126 $\times$ 75 $\times$ 75 grids with

$\Delta x = \Delta y = \Delta z = 0.31$ [mm]) and fine grids ($252 \times 150 \times 150$ grids with $\Delta x = \Delta y = \Delta z = 0.17$ [mm]). When a fracture crosses through the interface of grid cells, the crossing length and the aperture of the fracture were recorded. Substituting the crossing length and the aperture into the cubic law, the permeability on each grid interface was calculated in the following:

$$K_i = \frac{b^3 L}{12 A_i}, \quad i = x, y, z \tag{1}$$

where b is the fracture aperture, L is the crossing length on the interface, A is the cross-sectional area of the grids. We recorded all fractures in the calculation area and calculated the permeability in X, Y, Z directions on each grid interface. Those permeability on the grid surfaces is called "local permeability" in this study. Most of grids were crossed by a single fracture or without any fractures (85% of grids for using the coarse grids and 96% of grids for using the fine grids). Even when two or more fractures were intersected, the different representative values (e.g., arithmetic mean, area-weighted mean, length-weighted mean, largest value) were similar with other values. Thus, we used arithmetic area-weighted mean to determine local permeability on each grid interface. The porosity was determined as the ratio of the number of grids crossed by fractures to the total number of grids.

4. Comparison of Cross Sections

The cross sections of the 3-D printed samples and the computation design are shown in Figure 2. The left column in Figure 2 presents the images of the computational designs, and the center and right columns show the results of the sample treated with hexane and ethanol, respectively. The white parts reveal the fractures (void spaces), while the dark parts are the material heavier than the air (i.e., plastic and wax). Because the fracture network took account of the power law scaling for the fracture size, we can observe a variation of fracture aperture and fracture lengths in the computational designs and the CT images. As shown in Figures 2c, 2f, and 2i, only sparse fractures were observed in the CT images for the sample treated with ethanol. The created fractures were obviously fewer than the fractures in the computational design. The fractures existed only on the right side in the YZ slices (Figure 2f). This suggested that the wax remained in the sample and that removing the wax with ethanol was incomplete. On the other hand, the CT images of the sample treated with hexane (Figures 2b, 2e, and 2h) were similar to the images of the visualization of the computational design. As far as we can see, the hexane was effective in dissolving the wax in the sample, and the 3-D printer was able to reproduce the complex 3-D spatial distributions of fractures from the computational design.

Looking carefully between the computational design and CT images for the sample treated with hexane, some fractures existing in the computation design did not appear in the CT images. Some fractures in the computational design were longer than those in the CT images. The possible reasons were that the fracture was not printed out or that the wax was not removed completely.

In order to evaluate the accuracy of 3-D printed sample quantitatively, we compared the optical porosity from the CT images and from the computational design. The porosity was determined as a ratio of the number of white pixels to the total number of pixels. The optical porosities for CT images were obtained by using ImageJ (http://rsb.info.nih.gov/ij/) from digital images. ImageJ converts images to 8-bit color images with 256 colors and determines the thresholds between void spaces (white part) and the others. Note that the CT images required adjusting the thresholds by hand for each image, which may lead to some subjective errors.

We averaged the values by using 120 CT images of evenly spaced cross sections for XY, YZ and ZX slices. The optical porosity for computational images was obtained using Autodesk® Netfabb. The average was calculated using 2667 layer images. We also calculated the standard deviations for both CT images and computational images, which were plotted as the error bar.

The optical porosities are shown in Figure 3a. The average values were 18.2% for the sample treated with ethanol, 40.5% for the sample treated with hexane, and 40.2% for the computational design. We also measured the pore volume for the sample treated with hexane by using the displaced volume method, and determined it to be 5273.18 mm^3. The value from the CT scanner was 5957 mm^3, which was close to the measured value by the displaced volume method. These results indicate that posttreatment with hexane

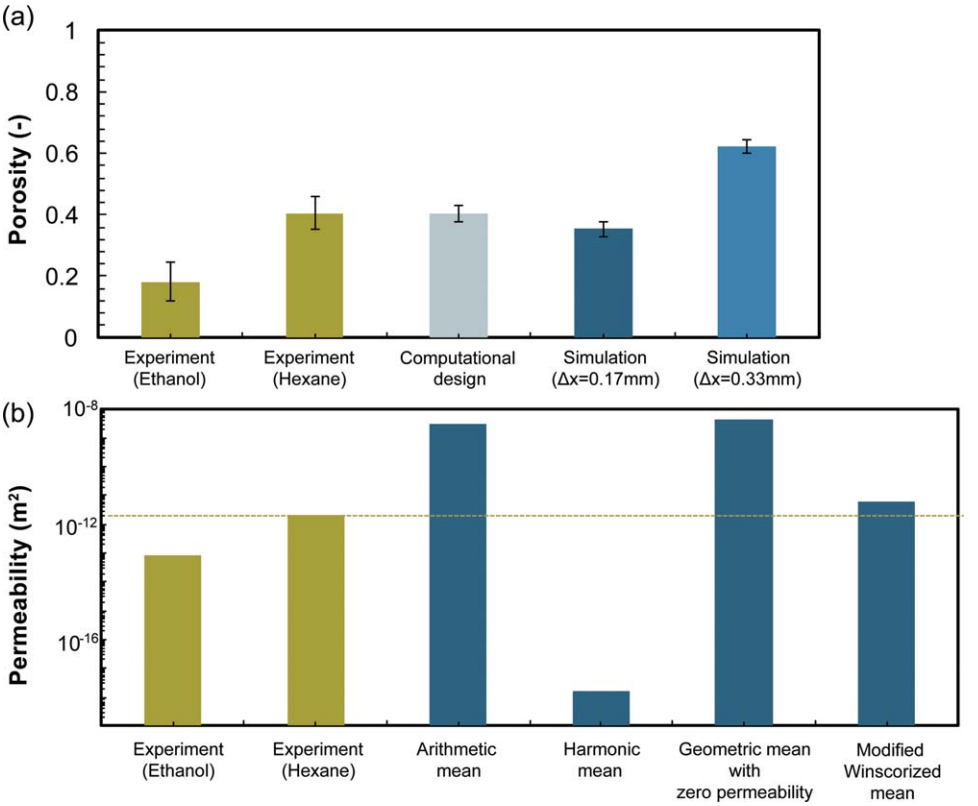

Figure 3. Comparison of hydraulic properties: (a) porosity and (b) permeability.

improved the dissolution of wax much better than ethanol and created almost the same pore space as the computational design.

The porosity of the computational design was slightly smaller than that of the sample treated with hexane. Because the pore volume measured by the sample was slightly smaller than CT scanning, the CT images could overestimate the porosity. The CT scanning determined either pore spaces or different materials by using the CT values, which was not a binary value but had some distribution. Thus, determining thresholds between the pore space and the solid may lead to some errors, and the porosity could be overestimated.

Figure 3a also presents the results of porosity for numerical simulation with coarse grids and fine grids, respectively. Larger grid cells resulted in overestimation of porosity in this numerical simulation. This result suggests that discretization in the simulation is sufficient with $\Delta x = 0.17$ mm.

5. Equivalent Permeability

5.1. Experimental Result

The average values with different hydraulic heads were 1.3×10^{-13} m^2 and 2.1×10^{-12} m^2 for the samples treated with ethanol and hexane, respectively. The permeability for the sample treated with hexane was 16 times higher than the permeability for the sample treated with ethanol. The Kozeny-Carman model [*Kozeny*, 1927; *Carman*, 1937] provides the estimated permeability from the values of the optical porosity in the following form:

$$K = C_{KC} \frac{\phi^3}{(1-\phi)^2} \tag{2}$$

where K is the permeability, and C_{KC} is the empirical parameter. ϕ is the porosity. The empirical parameter C_{KC} was calculated from the permeability and the porosity for the samples treated with ethanol, which was 1.44×10^{-11}. By using this value and the porosity for the samples treated with hexane, the permeability

was calculated to 2.7 $\times$ 10^{-12} m^2. This value was close to the measurement. The measurements for the porosity and the permeability were therefore confirmed to be reliable.

5.2. Numerical Calculation

The arithmetic, geometric, and harmonic mean of the local permeability were calculated by using simulation results. Figure 3b plots the arithmetic, geometric, and harmonic means as well as the experimental value from the sample treated with hexane. Although we obtained the local permeability tensor in three directions, there was no anisotropy of the permeability because the fractures orientations were random in this fracture network. Several studies suggest that arithmetic and harmonic means provide upper and lower bounds of equivalent permeability (i.e., Wiener bounds) [*Renard and de Marsily*, 1997]. As shown in Figure 3b, the experimental value (2.1 $\times$ 10^{-12} m^2) for the sample treated with hexane (dashed line) is between the arithmetic and harmonic means. This indicates that the Wiener bounds can be applied to the fracture network created by the 3-D printer.

Geometric mean is quite sensitive to regions with small permeability [e.g., *Jensen*, 1991]. For example, the geometric mean does not exist for discontinuous distributions with zero permeability. In this experiment, the base material for printing was impermeable acrylic plastic, which composed 60% of the sample. If the permeability of acrylic plastic is set to zero (as it is physically), the geometric mean cannot be obtained. We introduced two estimations to determine the modified geometric mean for equivalent permeability. First was to calculate the geometric mean without zero permeability. The frequency of local permeability was recalculated as the ratio of the grids where the value of the permeability was given to the grids with nonzero permeability. The data without zero permeability resulted in the geometric mean of 4.2 $\times$ 10^{-9} m^2. The frequency is in good agreement with log-normally distributed approximation. The trend is consistent with field observations [e.g., *Goggin and Chandler*, 1988]. The geometric mean using the log-normal approximation was 3.8 $\times$ 10^{-9} m^2. The value was close to the calculated value by using the exact frequency of permeability distribution (4.2 $\times$ 10^{-9} m^2). However, both the geometric means were higher than the experimental value (2.1 $\times$ 10^{-12} m^2). Neglecting the region of zero permeability overestimated the equivalent permeability.

The second way was to calculate the geometric mean by replacing grids with zero permeability to the smallest observed value, which is similar to the Winsorized mean but we only considered the lowest limit. The reason for this is that the symmetric Winsorized mean was not able to be calculated with zero permeabilty. The value of the modified Winsorized mean was 6.3 $\times$ 10^{-12} m^2, which is the same order as the experimental value (2.1 $\times$ 10^{-12} m^2). According to *Jensen* [1991], the Winsorized mean is less sensitive to small, possibly inaccurate, data values for log-normal permeability distribution. Thus, the modified Winsorized mean, which replaced zero permeability by the smallest values, could be a useful estimation for the equivalent permeability.

The experimental permeability was slightly smaller than the modified Winsorized mean obtained from the numerical model. Even if we succeeded in removing the wax almost completely, the 3-D printer was not able to create perfect fractures. For instance, the permeability in the numerical model assumed a parallel smooth surface of the fracture, while the printed fracture has rough surfaces because the 3-D printer created the sample while laminating layers in the vertical direction. This leads to stepwise surfaces. The roughness of the fractures could decelerate the flow and result in lower permeability than the numerical value.

The next step of this study aims to validate the numerical simulation method for fluid flow calculation including tracer transport. Although we used a fracture network with power-law scaling, other types of fracture network could be evaluated. The experimental results can help validate existing flow modeling and numerical methods.

6. Conclusions

We made a "rock" with a fracture network created using a 3-D printer and conducted flow tests. The CT scan images revealed that the 3-D printer was able to reproduce complex fracture networks accurately. The experimental value of permeability was between the arithmetic and harmonic mean of the local permeability given by the cubic law. The modified geometric mean was close to the experimental value, which is

consistent with conventional theoretical studies. Flow experiments using 3-D printed models can help validate existing theory, flow modeling, and numerical methods.

We need to mention that the "rock matrix" was impermeable in the 3-D printed fracture rocks and that the fracture roughness was probably different from that in real rocks. However, if we use 3-D printed fracture networks, we can: (i) know all of the fracture configurations, (ii) reproduce the same exact samples for subsequent experiments, and (iii) control the fracture parameters. 3-D printers allow us to create the fracture geometry of either actual distributions (i.e., CT scan images or outcrop photos) or any type of geometric models (i.e., geometric network or stochastic heterogeneity of petrophysical properties) repeatedly. By using the 3-D printed samples, we can conduct flow tests on the same physical configuration multiple times, even if a sample is contaminated or damaged during the experiment. The 3-D printer-based approach could be groundbreaking for geological studies.

Acknowledgments
This work was supported by the Japan Society for the Promotion of Science, under JSPS Postdoctoral Fellowships for JSPS Research Fellow (H28–8082), whose support is gratefully acknowledged. Requests for numerical and experimental data should be addressed to Anna Suzuki (e-mail: anna.suzuki@tohoku.ac.jp).

References

Bear, J. (1972), *Dynamics of Fluids in Porous Media*, Elsevier, New York.
Bour, O., and P. Davy (1997), Connectivity of random fault networks following a power law fault length distribution, *Water Resour. Res.*, *33*(7), 1567–1583.
Bour, O., and P. Davy (1999), Clustering and size distributions of fault patterns: Theory and measurements, *Geophys. Res. Lett.*, *26*(13), 2001–2004.
Bour, O., P. Davy, and C. Darcel (2002), A statistical scaling model for fracture network geometry, with validation on a multiscale mapping of a joint network (Hornelen Basin, Norway), *J. Geophys. Res.*, *107*(B6), 2113, doi:10.1029/2001JB000176.
Cacas, M. C., E. Ledoux, G. de Marsily, B. Tillie, A. Barbreau, E. Durand, B. Feuga, and P. Peaudecerf (1990), Modeling fracture flow with a stochastic discrete fracture network: Calibration and validation: 1. The flow model, *Water Resour. Res.*, *26*(3), 479–489, doi:10.1029/WR026i003p00479.
Carman, P. C. (1937), Fluid flow through granular beds, *Trans. Chem. Eng.*, *15*, 150–166, doi:10.1016/S0263-8762(97)80003-2.
Dagan, G. (1989), *Flow and Transport in Porous Formations*, Springer, New York.
Davy, P., R. Le Goc, C. Darcel, O. Bour, J. R. De Dreuzy, and R. Munier (2010), A likely universal model of fracture scaling and its consequence for crustal hydromechanics, *J. Geophys. Res.*, *115*, B10411, doi:10.1029/2009JB007043.
Goggin, D., and M. Chandler (1988), Patterns of permeability in Eolian Deposits: Page Sandstone (Jurassic), Northeastern Arizona, *SPE Form. Eval.*, *3*, 297–306, doi:10.2118/14893-PA.
Head, D., and T. Vanorio (2016), Effects of changes in rock microstructures on permeability: 3-D printing investigation, *Geophys. Res. Lett.*, *43*, 7494–7502, doi:10.1002/2016GL069334.
Ishutov, S., F. J. Hasiuk, C. Harding, and J. N. Gray (2015), 3D printing sandstone porosity models, *Interpreation*, *3*(3), SX49–SX61, doi:10.1190/INT-2014-0266.1.
Jafari, A., and T. Babadagli (2011), Effective fracture network permeability of geothermal reservoirs, *Geothermics*, *40*(1), 25–38, doi:10.1016/j.geothermics.2010.10.003.
Jensen, J. L. (1991), Use of the geometric average for effective permeability estimation, *Math. Geol.*, *23*(6), 833–840, doi:10.1007/BF02068778.
Jiang, Q., X. Feng, L. Song, Y. Gong, H. Zheng, and J. Cui (2016), Modeling rock specimens through 3D printing: Tentative experiments and prospects, *Acta Mech. Sin.*, *32*(1), 101–111, doi:10.1007/s10409-015-0524-4.
Ju, Y., H. Xie, Z. Zheng, J. Lu, L. Mao, F. Gao, and R. Peng (2014), Visualization of the complex structure and stress field inside rock by means of 3D printing technology, *Chin. Sci. Bull.*, *59*(36), 5354–5365, doi:10.1007/s11434-014-0579-9.
Ketcham, R. A., and W. D. Carlson (2001), Acquisition, optimization and interpretation of x-ray computed tomographic imagery: Applications to the geosciences, *Comput. Geosci.*, *27*(4), 381–400, doi:10.1016/S0098-3004(00)00116-3.
Kozeny, J. (1927), Uber kapillare Leitung der Wasser in Boden, *Sitzungsber. Akad. Wiss. Wien*, *136*, 271–306.
Long, C. T. O. and R. W. Zimmerman (2012), Estimating the hydraulic conductivity of two-dimensional fracture networks using network geometric properties, *Transp. Porous Media*, *93*(3), 777–797, doi:10.1007/s11242-012-9982-3.
Liu, R., Y. Jiang, B. Li, and X. Wang (2015), A fractal model for characterizing fluid flow in fractured rock masses based on randomly distributed rock fracture networks, *Comput. Geotech.*, *65*, 45–55, doi:10.1016/j.compgeo.2014.11.004.
Liu, R., B. Li, Y. Jiang, and N. Huang (2016), Review: Mathematical expressions for estimating equivalent permeability of rock fracture networks, *Hydrogeol. J.*, *24*, 1623–1649, doi:10.1007/s10040-016-1441-8.
Long, J. C. S., J. S. Remer, C. R. Wilson, P. A. Witherspoon (1982), Porous media equivalents for network of discontinuous fractures, *Water Resour. Res.*, *18*(3), 645–658, doi:10.1029/WR018i003p00645.
Miao, T., B. Yu, Y. Duan, and Q. Fang (2015), A fractal analysis of permeability for fractured rocks, *Int. J. Heat Mass Transfer*, *81*, 75–80, doi:10.1016/j.ijheatmasstransfer.2014.10.010.
Neuman, S. (1988), Stochastic continuum representation of fractured rock permeability as an alternative to the REV and fracture network concepts, *Groundwater Flow Qual. Model.*, *224*, 331–362, doi:10.1007/978-94-009-2889-3_19.
Odling, N. E., et al.(1999), Variations in fracture system geometry and their implications for fluid flow in fractured hydrocarbon reservoirs, *Pet. Geosci.*, *5*, 373–384.
Olasek, K., and P. Wiklak (2014), Application of 3D printing technology in aerodynamic study, XXI Fluid Mech. Conf. J. Phys. Conf. Ser., *530*(1), 12009, doi:10.1088/1742-6596/530/1/012009.
Olson, J. E. (2003), Sublinear scaling of fracture aperture versus length: An exception or the rule?, *J. Geophys. Res.*, *108*(B9), 2413, doi:10.1029/2001JB000419.
Pruess, K., and T. N. Narasimhan (1985), A practical method for modeling fluid and heat flow in fractured porous media, *SPEJ Soc. Pet. Eng. J.*, *25*(1), 14–26, doi:10.2118/10509-PA.
Renard, P., and G. de Marsily (1997), Calculating equivalent permeability: A review, *Adv. Water Resour.*, *20*(5–6), 253–278, doi:10.1016/S0309-1708(96)00050-4.

Schultz, R. A., C. Klimczak, H. Fossen, J. E. Olson, U. Exner, D. M. Reeves, and R. Soliva (2013), Statistical tests of scaling relationships for geologic structures, *J. Struct. Geol.*, *48*, 85–94, doi:10.1016/j.jsg.2012.12.005.

Suzuki, A., S. Sawasdee, H. Makita, T. Hashida, K. Li, and R. N. Horne (2016), Characterization of 3D printed fracture networks, paper presented at 41st Workshop on Geothermal Reservoir Engineering, Stanford University, Stanford, Calif.

Tsang, Y. W., C. F. Tsang, F. V Hale, and H. Rock (1996), Tracer transport in a stochastic continuum model of fractured media, *Water Resour. Res.*, *32*(10), 3077–3092.

Vermilye, J. M., and C. H. Scholz (1995), Relation between vein length and aperture, *J. Struct. Geol.*, *17*(3), 423–434, doi:10.1016/0191-8141(94)00058-8.

Warren, J. E., and H. S. Price (1961), Flow in heterogeneous porous media, *Soc. Pet. Eng. J.*, *1*(3), 153–169, doi:10.2118/1579-G.

Warren, J. E., and P. J. Root (1963), The behavior of naturally fractured reservoirs, *Soc. Pet. Eng. J.*, *3*(3), 245–255, doi:10.2118/426-PA.

Witherspoon, P. A., J. S. Y. Wang, K. Iwai, and J. E. Gale (1980), Validity of cubic law for fluid flow in a deformable rock fracture, *Water Resour. Res.*, *16*(6), 1016–1024.